NANO LETTERS

Letter

pubs.acs.org/NanoLett

Wide Wavelength Tuning of Optical Antennas on Graphene with Nanosecond Response Time

Yu Yao,[†] Mikhail A. Kats,[†] Raji Shankar,[†] Yi Song,[‡] Jing Kong,[‡] Marko Loncar,[†] and Federico Capasso*[,†]

[†]School of Engineering and Applied Sciences, Harvard University, Cambridge, Massachusetts, 02138, United States

[‡]Department of Electrical Engineering and Computer Science, Massachusetts Institute of Technology, Cambridge, Massachusetts 02139, United States

Supporting Information

ABSTRACT: Graphene is emerging as a broadband optical material which can be dynamically tuned by electrostatic doping. However, the direct application of graphene sheets in optoelectronic devices is challenging due to graphene's small thickness and the resultant weak interaction with light. By combining metal and graphene in a hybrid plasmonic structure, it is possible to enhance graphene–light interaction and thus achieve in situ control of the optical response. We show that the effective mode index of the bonding plasmonic mode in metal–insulator–metal (MIM) waveguides is particularly sensitive to the change in the optical conductivity of a graphene layer in the gap. By incorporating such MIM structures in optic antenna designs, we demonstrate an electrically tunable coupled antenna array on graphene with a large tuning range (1100 nm, i.e., 250 cm^{-1}, nearly 20% of the resonance frequency) of the antenna resonance wavelength at the mid-infrared (MIR) region. Our device exhibits a 3 dB cutoff frequency of 30 MHz, which can be further increased into the gigahertz range. This study confirms that hybrid metal–graphene structures are promising elements for high-speed electrically controllable optical and optoelectronic devices.

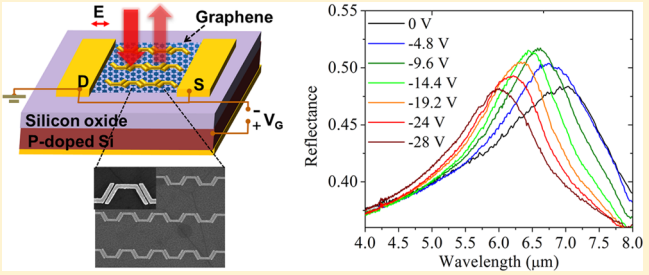

KEYWORDS: *Graphene, active plasmonics, coupled antennas, electrically tunable, high speed tuning*

The unique properties of optical antennas have enabled optical functionalities not available in natural materials and shown the potential to make a significant impact on photonic devices.[1−6] In situ control of the antenna resonances is highly desirable in many applications including multispectral detectors, biochemical sensors, spatial light modulators, and ultracompact optoelectronic devices. So far, a number of tuning methods based on thermal,[7,8] mechanical,[9] optical,[10] and electrical[11−21] mechanisms have been reported. In particular, electrical tuning has drawn a lot of attention as a promising route to the on-chip integration of subwavelength photonic components with electronics.[22] The prevailing electrical tuning mechanisms are based on phase-change media,[14,15] semiconductors,[16,17] liquid crystals,[18,19] and graphene.[13,20,21] Due to graphene's superior electrical and thermal conductivity, widely tunable electro-optical properties, material abundance, and good chemical resistance, it has substantial technological advantages in terms of fast response, broadband operation, compatibility with silicon technology, and large-scale fabrication.

Graphene is a monolayer of hexagonally arranged carbon atoms,[23] and its conductivity is strongly dependent on the Fermi level, which can be dynamically controlled by a gate voltage via electrostatic doping. The optical conductivity of graphene includes contributions from both interband and intraband transitions.[24] When the Fermi level is increased above half of the photon energy, the interband transitions are blocked, and intraband transitions dominate in the optical conductivity. Intraband transitions are highly sensitive to the charge carrier concentration in the graphene sheet; therefore the graphene optical conductivity (σ) and permittivity [$\varepsilon = 1 + (i\sigma(\omega)/\omega\varepsilon_0)$] show a strong dependence on the gate voltage,[24] which makes graphene a promising electrically tunable plasmonic material.[25−28] Here we exploit its tunable optical properties in the intraband-transition-dominated region to achieve electrical tuning of the optic antennas while suppressing the interband absorption in graphene. Although the optical response of graphene is widely tunable,[25,27−29] the resonances of plasmonic structures combined with graphene typically exhibit very limited tuning ranges[13,20,30] due to the fact that the graphene layer is atomically thin and thus only interacts with a very small portion of the plasmonic mode. One way to improve the graphene–light interaction is to incorporate graphene in the nanogap of the end-to-end coupled antennas, where the electric field is greatly enhanced.[31] Using such a structure with a 20 nm gap size, we have demonstrated a wavelength tuning range of the antenna resonance up to 650 nm (40% of the full-width at half-maximum (FWHM) of the resonance peak), a

Received: October 8, 2013
Revised: November 26, 2013
Published: December 3, 2013

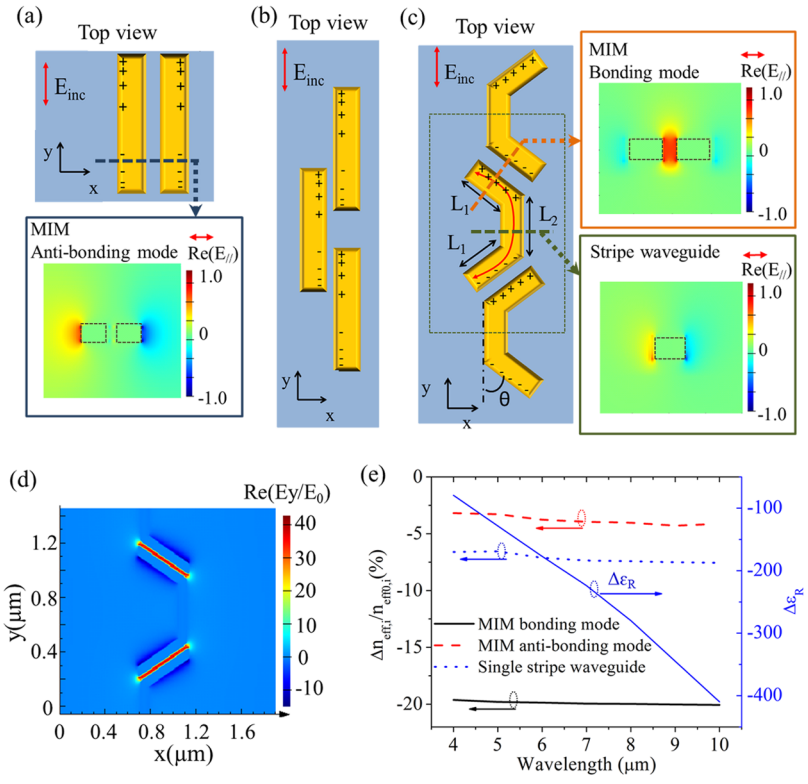

Figure 1. Design of the coupled antenna structure on graphene. (a) Top view of two identical linear rod antennas placed parallel to each other (top) and a cross-section view of the normalized amplitude of the electric field component parallel to the substrate surface $E_{\|}$ (the red arrow indicates the electric field polarization) of the MIM antibonding mode, obtained by a waveguide mode solver. Only the real part of the complex electric field amplitude is plotted, which is equivalent to a snapshot of the actual fields at some moment in time. The outline of the waveguide cross-section is given by dashed lines. The + and − signs indicate the instantaneous distribution of charges when the electromagnetic wave is incident vertically on the plane of the antennas with electrical field polarization along the *y*-axis. (b) Top view of identical linear rod antennas placed parallel and shifted with respect to each other along the *y*-axis. (c) Top view of the laterally coupled optic antennas with a bending angle θ on a graphene sheet (left) and the normalized electric field amplitudes ($E_{\|}$) of the MIM plasmonic bonding mode (right top) and the single-stripe plasmonic mode (right bottom). L_1 and L_2 are the lengths of the coupling sections and the single-stripe section, respectively. (d) Top view of the electric field amplitude enhancement $|E_{\|}/E_0|$ (E_0 is the electric field amplitude of the incident light) distribution at the middle plane of the coupled antenna structures in part c, obtained by finite difference time domain (FDTD) simulation (antenna length L_1 = 480 nm, L_2 = 480 nm, bending angle θ = 60°, gap size = 30 nm). (e) The calculated change in the real part of the graphene permittivity ($\Delta\varepsilon_R$) and the relative change in the effective mode indices ($\Delta n_{\mathrm{eff},i}/n_{\mathrm{eff0},i}$, $n_{\mathrm{eff0},i}$ is the effective mode index when the carrier concentration in the graphene sheet is ∼0) of the MIM bonding mode (i = B), the MIM antibonding mode (i = A), and the single-stripe waveguide mode (i = S) at different wavelengths, when the carrier concentration in graphene is increased from ∼0 to 1.2 × 10^{13} cm^{-2}. The gap size between coupling sections is chosen to be 30 nm in the calculations, the same as the smallest gap size achieved in our experiment. The graphene permittivity is calculated using the random phase approximation (RPA), and the experimentally measured graphene mobility (2000 $cm^{-2}/(V\ s)$ for our device before chemical doping) is used to obtain the carrier momentum relaxation time.[24]

300% increase compared to that of single antennas.[24] Yet, for many applications, for example, reconfigurable metasurfaces, a tuning range close to the FWHM of the antenna resonance peak is highly desirable to achieve a wide dynamic range in the intensity and phase of the antenna-scattered light. Although the end-to-end coupling approach is an effective way to enhance fields in subwavelength volumes,[32] further improvements in the resonance wavelength tuning range rely on technologically demanding gap sizes which are difficult to achieve with conventional fabrication methods. In this paper, we developed an antenna design strategy to enhance the interaction between the plasmonic mode and the underlying graphene along the antenna length. We also demonstrated antenna structures with a resonance wavelength tuning range of 1100 nm (80% of the resonance peak FWHM), almost twice of that achieved in end-to-end coupled antenna structures.[24]

Design. In general, the resonance wavelength of an optical antenna is determined by its dimensions and the surrounding medium. For example, the resonance wavelength of a single rod antenna can be calculated as[33]

$$\lambda_R = 2n_{\mathrm{eff}}L + \delta L \tag{1}$$

where L is the antenna length, n_{eff} is the effective mode index of the plasmonic waveguide mode propagating along the antenna, and δL is the contribution due to the reactance of the antenna ends, which is dependent on the shape and width of the antenna ends.[33] The permittivity of the medium surrounding the antenna affects both n_{eff} and δL. According to waveguide perturbation theory,[34] the change of the effective mode index Δn_{eff} due to a change in the surrounding medium permittivity $\Delta\varepsilon$ can be estimated from

$$\Delta n_{\mathrm{eff}} = \frac{n_{\mathrm{eff}}}{2}\sqrt{\frac{\varepsilon_0}{\mu_0}}\frac{\int_S \Delta\varepsilon\,|E|^2\,ds}{\int_S (\vec{E}\vec{H}^*)\cdot\hat{n}\,ds} \tag{2}$$

where S is the area of the waveguide cross section, E and H are the electric field and the magnetic field of the plasmonic

dx.doi.org/10.1021/nl403751p | Nano Lett. 2014, 14, 214−219

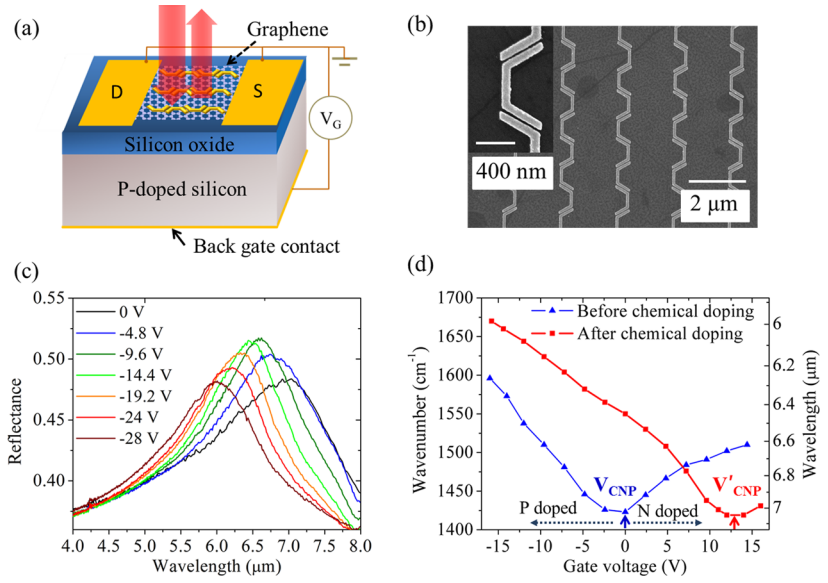

Figure 2. Device configuration and experimental results of the hybrid plasmonic structures (a) Schematic of the tunable plasmonic device with a back gate. (b) Scanning electron microscope (SEM) image of the plasmonic structure and a zoomed-in portion (antenna length L_1 = 480 nm, L_2 = 480 nm, bending angle = 60°, gap size = 30 nm, lateral period = 2 μm). (c) Measured reflection spectra from a device with antenna structures shown in part b after chemical doping of graphene for different gate voltages ($V_G - V_{CNP}$, V_{CNP} is the gate voltage when the concentrations of electrons and holes in the graphene sheet are equal). All spectra are normalized to the reflection spectra from a 300 nm Au film evaporated on the same silicon oxide substrate. (d) Measured (blue solid triangles: before chemical doping, red solid squares: after chemical doping) reflectance peak wavelengths for the same device as a function of gate voltage. Note the significantly larger tuning range after chemical doping. The arrows indicate the charge neutrality point voltage before and after chemical doping (V_{CNP} and V'_{CNP}).

waveguide mode, respectively (star * denotes the complex conjugate), and $\hat{n}$ represents the mode propagation direction. The most effective way to enhance the sensitivity of n_{eff} to changes of the graphene permittivity is to exploit plasmonic modes with a highly localized spatial distribution. It is well-known that the plasmonic bonding mode of a metal–insulator–metal (MIM) waveguide has a very high field concentration in the gap. If one incorporates elements of the MIM geometry into antennas by simply placing two identical linear antennas parallel to each other, the instantaneous charges on both sides of the gap are the same and accumulate on the outer sides of the two rods due to Coulomb repulsion (Figure 1a, top). This corresponds to the antibonding plasmonic mode in a MIM waveguide,[35,36] whose electric field has a node in the center of the gap, as shown on the bottom of Figure 1a. Because there is less field overlap in the gap, the change of the antibonding mode index ($\Delta n_{eff,A}$) due to a change in the graphene permittivity ($\Delta\varepsilon_R$) is an order of magnitude smaller compared to that of the bonding mode ($\Delta n_{eff,B}$) (Figure 1d). To instead utilize the bonding mode, we first shift the parallel antennas with respect to each other along the y-axis such that the bottom of one antenna is coupled with the top of another (Figure 1b). As a result, charges of opposite signs will tend to build up across the gap. This effect is magnified when the gap is small and the antennas are strongly coupled to each other and is further enhanced when the antenna ends are bent (Figure 1c) because the charges tend to accumulate on the outside edge of the antenna ends. A top view of the near field enhancement distribution of the structure is shown in Figure 1d for one period of the structure, which corresponds to the rectangular region enclosed by the dashed lines in Figure 1c. This field profile clearly shows the high field enhancement in the center of the antenna gaps, indicating that the bonding MIM plasmonic mode dominates.

The antenna resonance wavelength (λ_R) for the coupled antenna structure in Figure 1c, which has both MIM waveguide (bonding mode: $n_{eff,B}$) and single-stripe waveguide ($n_{eff,S}$) sections, can be calculated as

$$\lambda_R = 2n_{eff,B}(\lambda, V_G)L_1 + n_{eff,S}(\lambda, V_G)L_2 + \delta L \quad (3)$$

where L_1 and L_2 are the lengths of the coupling section and the single-stripe region, respectively. Equation 3 indicates that the tuning of the antenna resonance wavelength is proportional to the change of the mode refractive indices, $\Delta n_{eff,S}$ and $\Delta n_{eff,B}$. When the carrier concentration in the graphene sheet increases from 0 to 1.2 × 10^{13} cm^{-2}, the effective mode index of the single-stripe waveguide mode $\Delta n_{eff,S}$ decreases by about 7% (for the wavelength range from 4 to 10 μm), as shown in Figure 1e. By comparison, the index of the MIM bonding mode $n_{eff,B}$ is much more sensitive to the carrier concentration and decreases by ~20% for the same change of the carrier concentration in graphene. Therefore, the key to optimizing the antenna structures for a wide tuning range is to maximize the coupling section length L_1 while ensuring that the bonding mode dominates in the coupling sections. We performed FDTD simulation for structures with different coupling lengths (L_1) and bending angles (θ) and found that a structure with $L_1 \approx L_2$ and $\theta \approx 60°$ has the widest tuning range (see details in Supporting Information, part I). Moreover, a smaller gap size between the coupling sections results in an increased sensitivity of $n_{eff,B}$ to the change of graphene permittivity, and thus a wider tuning range, as will be discussed below.

Experiment. Figure 2a shows a schematic of the tunable plasmonic device. A graphene monolayer (confirmed by Raman spectra, see details in Supporting Information, part II) grown by atmospheric pressure chemical vapor deposition was transferred onto a 30 nm thermal oxide layer on a highly p-doped silicon substrate (0.001–0.005 Ω cm). A square area

dx.doi.org/10.1021/nl403751p | Nano Lett. 2014, 14, 214–219

(10^4 μm^2) of optic antennas and metal contacts (100 μm long, 10 μm wide) was patterned onto the graphene sheet by electron beam lithography (EBL), electron beam evaporation (5 nm Pd and 30 nm Au), and lift-off. Then unnecessary graphene (in the regions without plasmonic structures) was removed by oxygen plasma. For probing and bonding purposes, Ti/Au (20 nm/300 nm) pads (area: 7 × 10^4 μm^2) are evaporated onto the oxide layer, overlapping with the Pd/Au contacts. Then the gate contact (Ti/Au: 20 nm/300 nm) is evaporated onto the backside of the silicon substrate. Figure 2b shows the scanning electron microscopy (SEM) picture of a fabricated structure and the zoom-in over a small region.

The reflectance of our devices were measured using a Fourier transform infrared (FTIR) spectrometer with a MIR microscope (NA = 0.4) (see details in the Methods section).[24] Figure 2c shows the measured reflectance spectra from a device at different gate voltages. The wavelength of the reflectance peak (i.e., the antenna resonance wavelength) was tuned over about 1100 nm, 80% of the FWHM of the reflectance peak, which results in a phase tuning up to 1.2 radians around 6.5 μm and a modulation depth of the antenna-scattered light intensity of up to 70% around 7 μm. The wavelength of the reflectance peak is plotted in Figure 2d as a function of the applied voltage ($V_G - V_{CNP}$). The as-fabricated device exhibits a charge neutrality point voltage, V_{CNP}, around 0 V (see details in Supporting Information, part III). The dynamic range of the gate voltage V_G applied on the samples is limited to <16 V, due to the breakdown electric field of the gate dielectric (0.5–0.6 GV/m measured from the dry thermal oxide used in our experiment). After the graphene was chemically p-doped by immersing it in diluted nitric acid (HNO_3) (~5%, see details in the Methods section),[37] the charge neutrality point moved to a much higher voltage (V'_{CNP} = 13 V, see details in Supporting Information, part III), increasing the dynamic voltage range by 80%. The wavelength tuning range was increased by about 50% (from 750 to 1100 nm) compared to the tuning range before chemical doping (Figure 2d). Note that the tuning rate ($\Delta\lambda_R/\Delta V_G$) becomes smaller after chemical doping because it introduces additional scatterers into the graphene and decreases the carrier mobility. As a consequence, the real part of the graphene permittivity becomes less sensitive to the gate voltage (see details in Supporting Information, part IV).

In addition to the dynamic voltage range and the graphene carrier mobility, the gap size of the coupling region also affects the wavelength tuning range. Figure 3 shows that the change in the mode refractive index ($\Delta n_{eff,B}$) of the bonding mode in the MIM sections increases dramatically as the gap size decreases. Just like in a capacitor, the fringing fields outside of the antenna gap decrease with shrinking gap size, and thus more energy is concentrated inside the gap, resulting in a large $\Delta n_{eff,B}$ due to the enhanced interaction between the plasmonic mode and the graphene. According to eq 3, the resonance wavelength tuning range of the antenna ($\Delta\lambda$) is proportional to $\Delta n_{eff,B}$. Therefore, the wavelength tuning range also becomes larger as the gap size decreases, which is confirmed by the simulation and experimental results, as also shown in Figure 3. Moreover, FDTD simulation results show that the tuning range can be further increased to 2 μm (570 cm^{-1}, 40% of the antenna resonance) by improving fabrication methods to achieve structures with gap sizes ~10 nm. For gap sizes smaller than 10 nm, the quantum effect needs to be considered when calculating the optical conductivity of the graphene in the nanogaps,[38] which is beyond the scope of this paper.

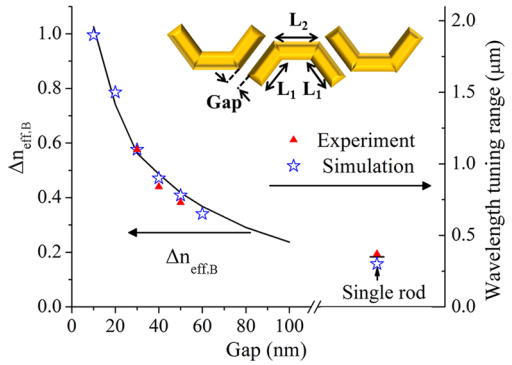

Figure 3. Wavelength tuning ranges of structures with different coupling gap sizes. Calculated effective mode refractive index change of bonding mode in the MIM waveguide (when the gate voltage increases from −16 to 16 V, solid black line) and wavelength tuning range (experiment: solid red stars; FDTD simulation: solid blue triangles) as a function of gap size ($L_1 = L_2$ = 480 nm, rod width 90 nm, bending angle 60°). Inset: schematic of lateral coupled antenna structures. The graphene permittivity used here is calculated using a carrier mobility of 1000 $cm^{-2}/(V\ s)$,[24] as measured in our device after chemical doping.

Note that in this work we investigate the tuning behavior of the antenna mode excited by light polarized along the *y*-axis. For incident light polarized along the *x*-axis, charges of the same sign accumulate at both sides of the gap, and therefore the antibonding mode dominates, which results in a very small tuning range (see more details in Supporting Information, part V).

The time response of the device was characterized by measuring frequency-dependent optical modulation at a fixed wavelength, as depicted in Figure 4a. As the antenna resonance is tuned away from its original wavelength λ_{R0} (corresponding to the maximum reflectance at graphene doping ~0 cm^{-2}), the reflectance at λ_{R0} decreases (see Figure 2c). Therefore, the response time can be obtained by measuring the modulation depth of the optical reflectance at λ_{R0} as a function of the modulation frequency of the gate voltage. The sine wave output of a function generator was connected to the back gate, and linear polarized light (polarization along the *y*-axis as shown in Figure 1c) from a continuous wave quantum cascade laser was directed onto the hybrid graphene–metal plasmonic structure. As the gate voltage changed, the reflection of the device varied, thus resulting in intensity modulation of the reflected light. The reflected light was collected onto a thermoelectrically cooled mercury cadmium telluride (MCT) detector (response time <10 ns). The output of the detector was measured with an oscilloscope to determine the optical modulation depth (the latter is defined as the peak amplitude of the sinusoidal signal divided by the DC level, more details are provided in the Supporting Information, part VI). The frequency-dependent optical modulation depth is shown in Figure 4b. A 3 dB cutoff frequency of 30 MHz for the optical modulation is obtained based on the measurement results.

To explore the factors that determine the modulation speed, we developed a small-signal, high-frequency circuit model of the device, shown in the inset of Figure 4b. In addition to the capacitances C_P (between the contact pads and back-gate) and C_G, the graphene resistance also plays an important role. In general, the most accurate way to model the electrical properties of graphene with the back-gate is a network of distributed resistors and capacitors. For simplification, here we

dx.doi.org/10.1021/nl403751p | Nano Lett. 2014, 14, 214–219

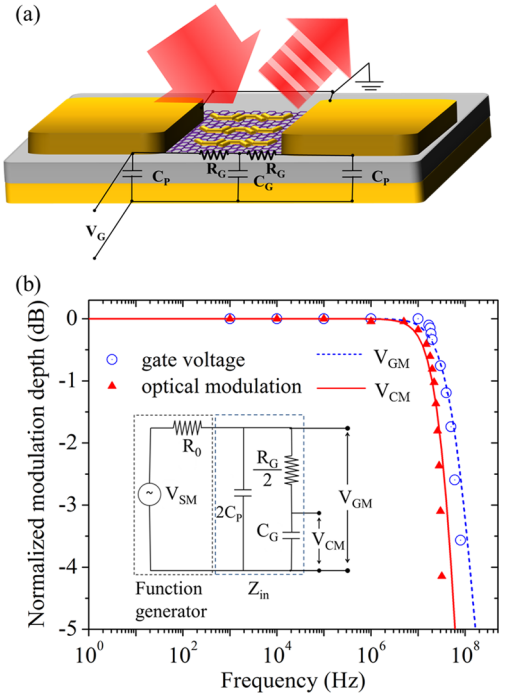

Figure 4. Small-signal frequency-response measurements. (a) Schematic of the frequency response measurement and the high-frequency circuit model of the sample. (b) Measured modulation depth of the optical reflectance and the gate voltage as a function of frequency, normalized to the low-frequency limit. The inset shows the small-signal high-frequency circuit model of the measurement setup. R_0 (50 Ω) is the internal impedance of the function generator.

only use R_G to represent the resistance of graphene sheet from the contact edge to the center of the graphene sheet and C_G to represent the capacitance between the graphene sheet and the back-gate. The output voltage signal from the function generator is $V_F = V_{DC} + V_{SM}\cos(\omega t)$. Since the output impedance of the function generator R_0 is finite, the amplitude of the applied gate voltage can be calculated based on the circuit model,

$$V_{GM} = V_{SM} \times \frac{((R_G/2) + (1/i\omega C_G))}{((R_G/2) + (1/i\omega C_G)) + R_0(i\omega 2C_P(R_G/2) + (2C_P/C_G) + 1)} \quad (4)$$

Due to the finite graphene resistance R_G, the modulation amplitude of the voltage on the contact pad V_{GM} is different from that of the potential in the center of the graphene sheet V_{CM}, as shown in the inset of Figure 4b. The modulation amplitude of the potential on the graphene sheet is

$$V_{CM} = V_{GM} \times \frac{1}{1 + i\omega C_G(R_G/2)} \quad (5)$$

The capacitances of our device were determined by $C-V$ measurements to be C_P = 50 pF and C_G = 6.6 pF. Based on electrical transport measurements, the graphene resistance R_G varies from 2.0 kΩ to 200 Ω depending on the gate voltage. We use R_G as a parameter to fit the measured frequency response of V_{GM} with eq 4. This gives a graphene resistance R_G = 600 Ω and a 3 dB cutoff frequency of 70 MHz. The frequency response of the calculated V_{CM} (eq 5) agrees well with that of the optical modulation. This indicates that the optical modulation cutoff frequency is limited by the circuit speed and not by the inherent limitation of the metal-graphene device.

Since $C_P \gg C_G$, eq 4 can be approximately written as

$$V_{GM} \approx V_{SM} \times \frac{1}{1 + i\omega 2C_P R_0} \quad (6)$$

Thus

$$V_{CM} \approx V_{SM} \times \frac{1}{1 + i\omega 2C_P R_0} \times \frac{1}{1 + i\omega C_G(R_G/2)} \quad (7)$$

From eq 7, we can see that there are two time constants, $\tau_{P0} = 2C_P R_0$ and $\tau_G = C_G R_G/2$, which determine the cutoff frequency of the V_{CM}. τ_{P0} can be decreased by shrinking the contact pad area and increasing the thickness of the insulating layer underneath the contact pad. τ_G can be decreased by increasing the thickness of the gate insulator and decreasing the graphene sheet area. Based on our calculation, a cutoff frequency up to 3 GHz is achievable in a practical device configuration (see details in Supporting Information, part VII).

Conclusion. We designed a new type of plasmonic structure comprised of closely coupled optical antennas such that field localization occurs along a significant portion of the antenna length rather than only at the ends. We showed that this type of structure interacts particularly strongly with monolayer graphene and that its plasmonic modes are significantly affected by the graphene optical properties which can be dynamically controlled by electrostatic doping. The antenna resonance wavelength can be tuned by as much as 1100 nm (250 cm^{-1}, 18% of the resonance frequency), almost twice as broad as the maximum tuning range achieved in previous works.[24] This type of metal−graphene structure can be used for tunable sensors, reconfigurable metasurfaces, and optical modulators or switches. In a broader context, the highly enhanced light−matter interaction at deep subwavelength scale in MIM-based optical antennas opens the door to a variety of highly compact optoelectronic devices.

Methods. *Modeling and Simulation.* In the FDTD simulations (Lumerical Solutions, Inc.), the graphene layer is modeled as an anisotropic material with in-plane permittivity $\varepsilon_{\parallel}$ and out of plane permittivity $\varepsilon_{\perp}$. The former is calculated from the graphene sheet optical conductivity,[24] and the latter is assumed to be 2.5.[39] The waveguide mode refractive index (defined as the waveguide mode propagation constant divided by the free space wavenumber) is also calculated with the same material parameters using a waveguide solver (Lumerical Solutions, Inc.). All other parameters are chosen to be the same as for the fabricated structures.

Chemical Doping Process for the Voltage-Tunable Antenna Structures on Graphene. To chemically dope the fabricated sample, we immerse it in diluted nitric acid (HNO_3, 5%) for 5 min, then rinse it in DI water for 30 s, followed by a nitrogen blow-dry.

Reflection Spectra Measurements. Spectral measurements were taken from an 80 μm × 80 μm aperture in a MIR microscope (Hyperion 2000). The frequency resolution is 2 cm^{-1}, and every spectrum is averaged over 100 scans.

■ ASSOCIATED CONTENT

Supporting Information

Coupling length and bending angle dependence of the antenna resonance wavelength tuning range, graphene growth and transfer, electrical transport characterization of graphene

dx.doi.org/10.1021/nl403751p | Nano Lett. 2014, 14, 214−219

sample, calculation of graphene permittivity, polarization dependence, derivation of modulation depth, and device design for a high cutoff frequency. This material is available free of charge via the Internet at http://pubs.acs.org.

AUTHOR INFORMATION

Corresponding Author

*E-mail: capasso@seas.harvard.edu Phone: 1-617-384-7611. Address: Pierce 205A, 29 Oxford Street, Cambridge, MA 02138.

Notes

The authors declare no competing financial interest.

ACKNOWLEDGMENTS

We gratefully acknowledge discussions with R. Blanchard, P. Genevet, D. Wolf, Y. Zhang, C. Wang, and J. MacArthur. Device fabrication was performed at the Center for Nanoscale Systems, which is a member of the National Nanotechnology Infrastructure Network supported by the National Science Foundation (NSF). This research is supported in part by the Air Force Office of Scientific Research under grant no. FA9550-12-1-0289 and by IARPA under grant N66001-13-1-2007 vice N66001-13-1-3005. M.L. and R.S. gratefully acknowledge the financial support by NSF via the collaborative research grant ECCS-1028519.

REFERENCES

(1) Yu, N. F.; Genevet, P.; Kats, M. A.; Aieta, F.; Tetienne, J. P.; Capasso, F.; Gaburro, Z. *Science* **2011**, *334*, 333−337.

(2) Stipe, B. C.; Strand, T. C.; Poon, C. C.; Balamane, H.; Boone, T. D.; Katine, J. A.; Li, J. L.; Rawat, V.; Nemoto, H.; Hirotsune, A.; Hellwig, O.; Ruiz, R.; Dobisz, E.; Kercher, D. S.; Robertson, N.; Albrecht, T. R.; Terris, B. D. *Nat. Photonics* **2010**, *4*, 484−488.

(3) Kinkhabwala, A.; Yu, Z. F.; Fan, S. H.; Avlasevich, Y.; Mullen, K.; Moerner, W. E. *Nat. Photonics* **2009**, *3*, 654−657.

(4) Challener, W. A.; Peng, C. B.; Itagi, A. V.; Karns, D.; Peng, W.; Peng, Y. Y.; Yang, X. M.; Zhu, X. B.; Gokemeijer, N. J.; Hsia, Y. T.; Ju, G.; Rottmayer, R. E.; Seigler, M. A.; Gage, E. C. *Nat. Photonics* **2009**, *3*, 220−224.

(5) Tang, L.; Kocabas, S. E.; Latif, S.; Okyay, A. K.; Ly-Gagnon, D. S.; Saraswat, K. C.; Miller, D. A. B. *Nat. Photonics* **2008**, *2*, 226−229.

(6) Anker, J. N.; Hall, W. P.; Lyandres, O.; Shah, N. C.; Zhao, J.; Van Duyne, R. P. *Nat. Mater.* **2008**, *7*, 442−453.

(7) Xu, G.; Huang, C. M.; Tazawa, M.; Jin, P.; Chen, D. M. *J. Appl. Phys.* **2008**, *104*, 053102.

(8) Kats, M. A.; Blanchard, R.; Genevet, P.; Yang, Z.; Qazilbash, M. M.; Basov, D. N.; Ramanathan, S.; Capasso, F. *Opt. Lett.* **2013**, *38*, 368−370.

(9) Huang, F. M.; Baumberg, J. J. *Nano Lett.* **2010**, *10*, 1787−1792.

(10) Abb, M.; Albella, P.; Aizpurua, J.; Muskens, O. L. *Nano Lett.* **2011**, *11*, 2457−2463.

(11) Kossyrev, P. A.; Yin, A. J.; Cloutier, S. G.; Cardimona, D. A.; Huang, D. H.; Alsing, P. M.; Xu, J. M. *Nano Lett.* **2005**, *5*, 1978−1981.

(12) Berthelot, J.; Bouhelier, A.; Huang, C. J.; Margueritat, J.; Colas-des-Francs, G.; Finot, E.; Weeber, J. C.; Dereux, A.; Kostcheev, S.; El Ahrach, H. I.; Baudrion, A. L.; Plain, J.; Bachelot, R.; Royer, P.; Wiederrecht, G. P. *Nano Lett.* **2009**, *9*, 3914−3921.

(13) Kim, J.; Son, H.; Cho, D. J.; Geng, B. S.; Regan, W.; Shi, S. F.; Kim, K.; Zettl, A.; Shen, Y. R.; Wang, F. *Nano Lett.* **2012**, *12*, 5598−5602.

(14) Driscoll, T.; Kim, H. T.; Chae, B. G.; Kim, B. J.; Lee, Y. W.; Jokerst, N. M.; Palit, S.; Smith, D. R.; Di Ventra, M.; Basov, D. N. *Science* **2009**, *325*, 1518−1521.

(15) Samson, Z. L.; MacDonald, K. F.; De Angelis, F.; Gholipour, B.; Knight, K.; Huang, C. C.; Di Fabrizio, E.; Hewak, D. W.; Zheludev, N. I. *Appl. Phys. Lett.* **2010**, *96*, 143105.

(16) Chen, H. T.; Padilla, W. J.; Zide, J. M. O.; Gossard, A. C.; Taylor, A. J.; Averitt, R. D. *Nature* **2006**, *444*, 597−600.

(17) Chan, W. L.; Chen, H. T.; Taylor, A. J.; Brener, I.; Cich, M. J.; Mittleman, D. M. *Appl. Phys. Lett.* **2009**, *94*, 213511.

(18) Zhao, Q.; Kang, L.; Du, B.; Li, B.; Zhou, J.; Tang, H.; Liang, X.; Zhang, B. Z. *Appl. Phys. Lett.* **2007**, *90*, 011112.

(19) Buchnev, O.; Ou, J. Y.; Kaczmarek, M.; Zheludev, N. I.; Fedotov, V. A. *Opt. Express* **2013**, *21*, 1633−1638.

(20) Emani, N. K.; Chung, T. F.; Ni, X. J.; Kildishev, A. V.; Chen, Y. P.; Boltasseva, A. *Nano Lett.* **2012**, *12*, 5202−5206.

(21) Lee, S. H.; Choi, M.; Kim, T. T.; Lee, S.; Liu, M.; Yin, X.; Choi, H. K.; Lee, S. S.; Choi, C. G.; Choi, S. Y.; Zhang, X.; Min, B. *Nat. Mater.* **2012**, *11*, 936−941.

(22) Zheludev, N. I.; Kivshar, Y. S. *Nat. Mater.* **2012**, *11*, 917−924.

(23) Novoselov, K. S.; Geim, A. K.; Morozov, S. V.; Jiang, D.; Katsnelson, M. I.; Grigorieva, I. V.; Dubonos, S. V.; Firsov, A. A. *Nature* **2005**, *438*, 197−200.

(24) Yao, Y.; Kats, M. A.; Genevet, P.; Yu, N. F.; Song, Y.; Kong, J.; Capasso, F. *Nano Lett.* **2013**, *13*, 1257−1264.

(25) Ju, L.; Geng, B. S.; Horng, J.; Girit, C.; Martin, M.; Hao, Z.; Bechtel, H. A.; Liang, X. G.; Zettl, A.; Shen, Y. R.; Wang, F. *Nat. Nanotechnol.* **2011**, *6*, 630−634.

(26) Yan, H. G.; Low, T.; Zhu, W. J.; Wu, Y. Q.; Freitag, M.; Li, X. S.; Guinea, F.; Avouris, P.; Xia, F. N. *Nat. Photonics* **2013**, *7*, 394−399.

(27) Chen, J. N.; Badioli, M.; Alonso-Gonzalez, P.; Thongrattanasiri, S.; Huth, F.; Osmond, J.; Spasenovic, M.; Centeno, A.; Pesquera, A.; Godignon, P.; Elorza, A. Z.; Camara, N.; de Abajo, F. J. G.; Hillenbrand, R.; Koppens, F. H. L. *Nature* **2012**, *487*, 77−81.

(28) Fei, Z.; Rodin, A. S.; Andreev, G. O.; Bao, W.; McLeod, A. S.; Wagner, M.; Zhang, L. M.; Zhao, Z.; Thiemens, M.; Dominguez, G.; Fogler, M. M.; Neto, A. H. C.; Lau, C. N.; Keilmann, F.; Basov, D. N. *Nature* **2012**, *487*, 82−85.

(29) Yan, H. G.; Low, T.; Zhu, W. J.; Wu, Y. Q.; Freitag, M. L., Li, X. S.; Guinea, F., Avouris, P.; Xia, F. N. *arXiv:1209.1984* **2012**.

(30) Mousavi, S. H.; Kholmanov, I.; Alici, K. B.; Purtseladze, D.; Arju, N.; Tatar, K.; Fozdar, D. Y.; Suk, J. W.; Hao, Y. F.; Khanikaev, A. B.; Ruoff, R. S.; Shvets, G. *Nano Lett.* **2013**, *13*, 1111−1117.

(31) Muhlschlegel, P.; Eisler, H. J.; Martin, O. J. F.; Hecht, B.; Pohl, D. W. *Science* **2005**, *308*, 1607−1609.

(32) Yu, N.; Cubukcu, E.; Diehl, L.; Belkin, M. A.; Crozier, K. B.; Capasso, F.; Bour, D.; Corzine, S.; Hofler, G. *Appl. Phys. Lett.* **2007**, *91*, 173113.

(33) Novotny, L. *Phys. Rev. Lett.* **2007**, *98*, 266802.

(34) Johnson, S. G.; Ibanescu, M.; Skorobogatiy, M.; Weisberg, O.; Engeness, T. D.; Soljacic, M.; Jacobs, S. A.; Joannopoulos, J. D.; Fink, Y. *Opt. Express* **2001**, *9*, 748−779.

(35) Woolf, D.; Loncar, M.; Capasso, F. *Opt. Express* **2009**, *17*, 19996−20011.

(36) Zia, R.; Selker, M. D.; Catrysse, P. B.; Brongersma, M. L. *J. Opt. Soc. Am. A* **2004**, *21*, 2442−2446.

(37) Kasry, A.; Kuroda, M. A.; Martyna, G. J.; Tulevski, G. S.; Bol, A. A. *ACS Nano* **2010**, *4*, 3839−3844.

(38) Thongrattanasiri, S.; Manjavacas, A.; de Abajo, F. J. G. *ACS Nano* **2012**, *6*, 1766−1775.

(39) Falkovsky, L. A. *J. Phys.: Conf. Ser.* **2008**, *129*, 012004.